Effects of self-limiting oxide layer on optical and electronic properties of WTe2 for optoelectronic applications

Tang, Hongyu; Shi, Weiqi; Ding, Yifan; Qi, Jiao; Wu, Shuai; Liu, Weiming; Wang, Gaoyuan; Fan, Jiajie; Zhang, Rongjun; Zhang, Guoqi

DOI
10.1016/j.apsusc.2024.161913

Publication date
2025

Document Version
Final published version

Published in
Applied Surface Science

Citation (APA)
Tang, H., Shi, W., Ding, Y., Qi, J., Wu, S., Liu, W., Wang, G., Fan, J., Zhang, R., & Zhang, G. (2025). Effects of self-limiting oxide layer on optical and electronic properties of WTe2 for optoelectronic applications. *Applied Surface Science*, *684*, Article 161913. https://doi.org/10.1016/j.apsusc.2024.161913

Applied Surface Science 684 (2025) 161913

Contents lists available at ScienceDirect

Applied Surface Science

journal homepage: www.elsevier.com/locate/apsusc

Full Length Article

Effects of self-limiting oxide layer on optical and electronic properties of WTe_2 for optoelectronic applications

Hongyu Tang [a,*], Weiqi Shi [a], Yifan Ding [b], Jiao Qi [b], Shuai Wu [c], Weiming Liu [b], Gaoyuan Wang [a], Jiajie Fan [a], Rongjun Zhang [a,b,*], Guoqi Zhang [d]

[a] Academy for Engineering and Technology, Fudan University, Shanghai 200433, China
[b] Department of Optical Science and Engineering, Key Laboratory of Micro and Nano Photonic Structures (MOE), Shanghai Engineering Research Center of Ultra-Precision Optical Manufacturing, Fudan University, Shanghai 200433, China
[c] School of Mechanical Engineering, Hebei University of Technology, Tianjin 300401, China
[d] EEMCS Faculty, Delft University of Technology, Delft 2628CD, the Netherlands

ARTICLE INFO

Keywords:
Weyl Semi-Metal Tungsten Ditelluride (WTe_2)
Self-limiting oxide (SLO)
Optical and electronic properties
Positive and negative photocurrent

ABSTRACT

The study focuses on the optical and electrical properties of Tungsten Ditelluride (WTe_2), a type II Weyl semimetal, as well as the influence of its self-limiting oxide (SLO) layer that forms during natural oxidation. WTe_2 exhibits promising applications in photodetection and energy harvesting due to its unique gapless linear dispersion and Berry-field-enhanced nonlinear optical effects. However, surface oxidation poses a challenge as it degrades the performance of WTe_2. By employing spectroscopic ellipsometry and Raman spectroscopy, the progression of the oxide layer's thickness and its impact on the optical constants of WTe_2 were examined. The results revealed a rapid increase in oxide thickness within the first 24 h, and it reached saturation at ~10 nm after 45 h of atmospheric exposure. Electrical properties were explored using Kelvin Probe Force Microscopy, uncovering a modification in surface potential and Fermi level following oxidation. Additionally, a SLO/WTe_2 heterojunction device exhibited a wide region of positive and negative coexisting photocurrent, highlighting the potential for logical operations in ambient air. Finally, the mechanism of operation of the device is discussed. The electrical and optical properties of the pristine, partially oxidized and fully oxidized WTe_2 are analyzed using density functional theory calculations. It shows that the SLO layer has a significant effect on the optical and electronic properties, which is instructive for future wavelength-modulated device optoelectronic logic operations.

1. Introduction

Optical sensing and energy harvesting technologies, leveraging the distinctive properties and innovative working principles of quantum materials such as Weyl semimetals (WSMs), hold immense potential to transcend the inherent performance constraints of conventional photodetectors and solar cells [1–4]. T_d-WTe_2, a type II WSM, exhibits promising applications in photodetection and energy harvesting due to its gapless linear dispersion and Berry-field-amplified nonlinear optical effects near the Weyl nodes [5,6]. Rano *et al.* [7] utilized reflectance spectroscopy to demonstrate that WTe_2 and $MoTe_2$ composites are excellent reflective materials across a broad energy spectrum, from infrared to ultraviolet, with effective ultraviolet radiation absorption capabilities. Wang *et al.* [8] found that, due to the crystal symmetry breaking along certain crystal fracture directions and strong Fermi arc-type surface states, T_d-WTe_2 exhibits a robust and universal edge current response across a wide wavelength range of laser illumination. However, implementing an external bias on WSM-based photodetectors is impractical, as it can induce a significant dark current in conducting materials even in the absence of light. Fortunately, van der Waals (vdW) heterojunctions based on WSMs can effectively suppress the dark current, greatly extend the detection range, and improve the light absorption efficiency and response speed. Feng *et al.* [9] proposed a self-powered Pd-WTe_2-Ag photoconductive diode which was sensitive to a wide spectral range (λ = 320–1200 nm). Based on a 2D Dirac/Weyl semimetallic heterostructure, Liu *et al.* [10] reported graphene/WTe_2 phototransistors with a photoresponsivity of 8.7 A/W under 650 nm laser irradiation. Wang *et al.* [11] investigated a 1 T′-WTe_2/bulk GaAs

* Corresponding authors at: Academy for Engineering and Technology, Fudan University, Shanghai 200433, China (H. Tang and R. Zhang).
E-mail addresses: hongyu_tang@fudan.edu.cn (H. Tang), rjzhang@fudan.edu.cn (R. Zhang).

https://doi.org/10.1016/j.apsusc.2024.161913
Received 31 August 2024; Received in revised form 10 November 2024; Accepted 22 November 2024
Available online 23 November 2024

vdW vertical Schottky diode, which has a rectification ratio of more than 10^3 and can respond to the wavelength range of 400–1100 nm.

Despite these advancements, all aforementioned optoelectronic devices incorporate a protective layer to safeguard WTe_2 from air-induced oxidation. Surface oxidation layers introduce disorder, impairing electronic charge transport, suppressing the intrinsic properties of WTe_2, and ultimately degrading device performance. Lee *et al.* [12] conducted experimental and theoretical studies on the electronic properties of WTe_2, confirming that T_d-WTe_2 is prone to environmental oxidation. Hou *et al.* [13] combined atomic force microscopy (AFM), Raman spectroscopy, and ellipsometry measurements to report the formation and dynamics of surface oxides in WTe_2 crystals. Their findings revealed the formation of a ~2.5 nm thick self-limiting oxide (SLO) layer after several hours of atmospheric exposure, generating WOx ($2 < x < 3$) and TeO_2 as oxidation products. These oxidation products remain stable in air and thus effectively halt further spontaneous oxidation. While the SLO layer prevents further oxygen diffusion, its impact on the optical and electronic properties of WTe_2 remains unexplored.

Therefore, it is necessary to analyze the effects of SLO Layer on the optical and electronic properties of WTe_2 and explore its potential optoelectronic applications in ambient air. In this paper, we address this gap by analyzing the effects of the SLO layer on electronic and the optical properties of WTe_2, and optoelectronic response. Firstly, we employ spectroscopic ellipsometry and Raman spectroscopy to assess the evolution of the oxide layer's thickness and its resultant influence on the optical constants of WTe_2. Secondly, we delve into the electronic properties using Kelvin Probe Force Microscopy (KPFM), revealing modifications in surface potential and Fermi level post-oxidation. Furthermore, we test the photocurrent map of a SLO/WTe_2 heterojunction device in ambient air, aiming to explore its viability for optoelectronic logic operations.

2. Materials and methods

2.1. Device Fabrication

WTe_2 flakes were mechanically exfoliated from the bulk material (SixCarbon Technology Shenzhen) and then transferred to 300 nm SiO_2/Si substrates. The exfoliated WTe_2 flakes with different thicknesses were transferred to the top of metal electrodes by the dry-transfer method. Then, they were exposed to air for several hours to form the SLO layer and obtained the SLO/WTe_2 heterostructures-based devices.

2.2. Characterizations

Spectroscopic ellipsometry (SE; J. A. Woollam Inc. M2000X-FB-300XTF) was employed in the wavelength region of 200–1000 nm at a fixed incident angle of 65∘ to explore the optical properties of the WTe_2 before and after oxidation. The SE fitting process was achieved by CompleteEASE software. The Raman and photoluminescence (PL) spectra were conducted at room temperature with a 532 nm laser excitation on a WITec alpha300R Confocal Raman Microscope and a grating of 1800 lines/mm. The measurements were performed with a laser power of 1 mW and with a spot size of ~0.5 μm. The contact potential difference (CPD) between a Kelvin probe and a heterostructured optoelectronic device was examined using the MFP-3D atomic force microscope (AFM) system, produced by Asylum Research. The morphology was initially characterized using the AC Air Topograph mode, and subsequently, surface potential images were obtained using the Scanning Kelvin Probe Microscopy (SKPM) mode. During this process, a direct current (DC) voltage of + 3 V was applied to the tip. The probe model utilized was the ASYELEC-01-R2, which features a platinum/iridium (Pt/Ir) coating on the tip surface, a typical tip radius of 25 nm, and a scan rate of 1 Hz. The photoelectrical characterization was done by using a home-built set-up with one Keithley 2636 source meter. The source meter was used for applying source-drain bias (V_{ds}).

2.3. Computational methods

All first-principles calculations regarding the structural relaxation, electronic properties, and optical properties of both pristine and oxidized T_d-WTe_2 are performed by employing Density Functional Theory (DFT) as implemented in the plane-wave code CASTEP [14,15]. The exchange and correlation energies in our calculations are implemented using generalized gradient approximation (GGA) and Perdew-Burke-Ernzerhof (PBE) functionals [16]. Double numerical atomic orbital plus polarization (DNP) is chosen as the basis set, and the global orbital cut-off is set to 5.0 Å. To avert interlayer interactions, two adjacent slabs are separated by a perpendicular vacuum of 15 Å. Spin polarization is included in the computations. A $12 \times 12 \times 1$ k-points mesh is utilized for geometric optimization and accurate calculation of electronic properties. The maximum energy force and convergence tolerance settings are 0.002 Ha/A and 1.0×10^{-6} Ha respectively. All structures are fully relaxed using the conjugate gradient method until the convergence values of total energy and Hellmann-Feynman force are less than 10^{-5} eV and 0.02 eV/Å respectively. For structure relaxation and reaction calculations, Monkhorst-Pack k-point meshes of $10 \times 20 \times 5$ and $4 \times 2 \times 1$ are employed respectively. In terms of optical properties, the plane wave energy cut-off value is set to 450 eV. In addition, the frequency-dependent dielectric matrix was calculated by using the Fermi golden rule within the dipole approximation. We calculated the imaginary part of the dielectric function (ε_2) of monolayer WTe_2 before and after oxidation, which relates to its optical properties and is defined as,

$$\varepsilon_2(\omega) = \frac{4\pi^2 e^2}{\Omega\omega^2} \sum_{k,c,v} \left| \langle \psi_k^c | u \bullet r | \psi_k^v \rangle \right|^2 \delta\left(E_k^c - E_k^v - E\right) \quad (1)$$

where Ω is the volume of the unit cell, ω is the frequency of the incident photon, e is electronic charge, ψ_k^c and ψ_k^v are the quantum states of electrons in the conduction and valence bands, respectively, with a momentum given by (h/2π)k.

3. Results and discussion

3.1. Self-limiting oxide (SLO) layer formation on the top of WTe_2

To quantitatively determine the thickness of the surface oxide, spectroscopic ellipsometry measurements were conducted in ambient conditions, encompassing a wavelength spectrum ranging from 300 to 2500 nm, with incremental steps of approximately 10 nm. These measurements were executed in terms of tanΨ and cosΔ. The phase shifts and amplitude fluctuations were respectively articulated through the angles Psi (Ψ) and Del (Δ). Subsequent to acquiring a freshly exfoliated WTe_2 nanosheet via mechanical means, measurements were conducted at selected time intervals spanning from 0 to 200 h. Fig. 1 shows the evolution of the oxide layer thickness of WTe_2 over time and the corresponding optical constants. Fig. 1a illustrates the values of Ψ and Δ for the freshly peeled WTe_2 sample as a function of wavelength at 0 h (measured immediately after exfoliations). Fig. 1b presents the subsequently recorded data and its comparison with the initial data. The experimental data were fitted by the Cauchy model, assuming that no surface oxides were present on the freshly prepared surface. At the inception of oxidation, the thickness undergoes a relatively rapid change. It attains 9 nm after 24 h and reaches saturation at approximately 10 nm after 45 h of atmospheric exposure. This aligns with previously reported trends, indicative of a typical self-limiting oxidation process. However, the thickness of SLO observed here surpasses that reported by Hou [13]. The thickness versus time data can be fitted with the following function:

$$T(\mathrm{nm}) = T_{max}(\mathrm{nm})(1 - e^{-k_1 \bullet t(\mathrm{h})}) \quad (2)$$

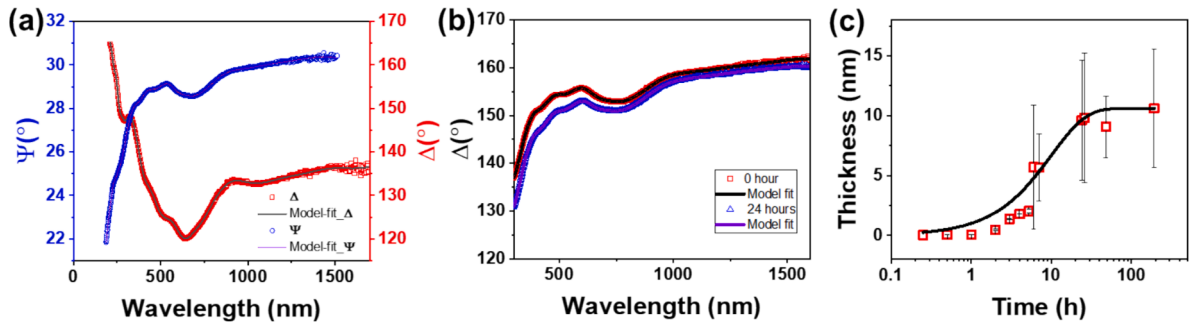

Fig. 1. Evolution of the oxide layer thickness of WTe_2 measured by spectroscopic ellipsometry in an ambient atmosphere and related optical constants. (a) Psi (Ψ) and Del (Δ) values of the freshly peeled WTe_2 sample as a function of wavelength. (b) Comparison of Δ values measured at 0 and 24 h. The experimental data in (a) and (b) are fitted with the Cauchy model. (c) Thickness of the oxide layer as a function of time.

Here, T_{max} represents the saturated thickness of the oxidation layer, while k_1 denotes the time constant, reflecting the rate of change in oxide layer thickness. As depicted in Fig. 1c, T_{max} is ~10 nm, and k_1 is 0.1 h^{-1}.

Previous studies [13,17] have demonstrated that both the Raman peak intensity and light absorption of pristine WTe_2 diminish over time, with surface oxidation identified as the underlying cause. For the purpose of comparatively analyzing the effect of oxidation in air on WTe_2 with different thicknesses, four points (P1, P2, P3, and P4) of varying thicknesses were selected for Raman spectroscopy (see Fig. 2a). As depicted Fig. 2b, the Raman spectrum of the freshly exfoliated WTe_2 encompasses main Raman peaks A_1^3, A_1^4, A_1^7 and A_1^9 (in the range between 100–250 cm^{-1}) [18–20]. The thicknesses of P1 – P4, as measured by

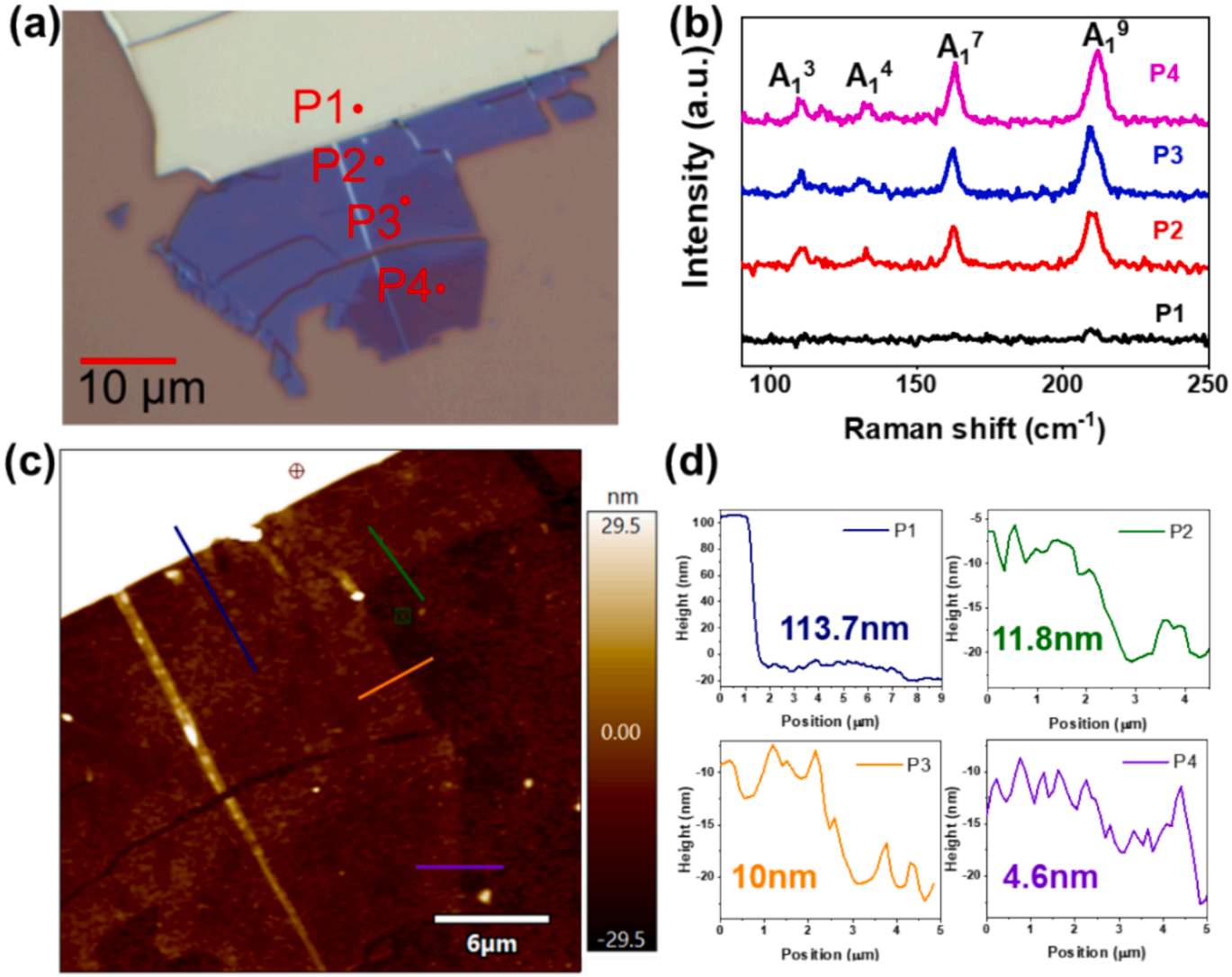

Fig. 2. WTe_2 crystal structure and Raman spectra of WTe_2 with different thickness. a) Optical microscope image of the fresh peeled WTe_2 flake with different thickness. Scale bar: 10 μm. b) Measured Raman spectra of the fresh peeled WTe_2 flake at positions of P1, P2, P3, and P4. c) AFM morphology images of the fresh peeled WTe_2 flake. d) Corresponding thickness at positions of P1, P2, P3, and P4.

AFM, are 113.7 nm, 11.8 nm, 10 nm, and 4.6 nm, respectively (see Fig. 2c and d). The A_1^7 mode causes Te atoms to vibrate along the c-axis, while the A_1^9 mode makes W atoms vibrate along the c-axis [21]. Obviously, the thicker the WTe_2 nanoflake, the weaker the Raman signal. Fig. 3a and b show the Raman results for different thicknesses of WTe_2 exposed to ambient conditions for 192 h, respectively. The intensity of all the samples decreased significantly after exposure to ambient conditions, indicating that WTe_2 degraded during this time. Both of A_1^7 and A_1^9 modes are significantly influenced by surface degradation, the intensity of the peaks diminishes over time. Additionally, other Raman peaks A_1^3, A_1^4 (in the range of 100–150 cm^{-1}) completely disappear within a few hours after the start of the measurement.

Fig. 3e shows the Raman peak intensities for each thickness of WTe_2 with degradation time. All the samples showed no obvious Raman peak position shift at the beginning of the degradation process, and a small amount of oxide layers were produced without either obvious tension changes or interlayer van der Waals interactions. After 28 h, the Raman peaks were obviously red-shifted, indicating that the arrangement of atoms or molecules became disordered when the SLO layer was thickened, the vibration was less constrained, the vibration frequency was reduced, and the Raman peaks were red-shifted. We found that the intensities of both A_1^7 and A_1^9 modes decay significantly during the degradation process. We then fitted the peak intensities with the following exponential decay function,

$$I(t) = I_1 e^{-\frac{t}{\tau}} + I_2 \tag{3}$$

where I_1 is the initial Raman peak intensity, I_2 is the intensity after saturation of degradation, t is the time interval between the current Raman measurement and the flake after fresh exfoliation, and τ is the characteristic time of intensity decay, respectively. The decay time of the samples at the thicknesses of P1-P4 is in the range of 18–25 h. After 117 h, most of the Raman signals disappear, and combined with the ellipsometric spectroscopy results, it can be inferred that the degradation of WTe_2 occurs mainly on its surface, which is a self-limiting and saturating behaviour. These degradations are consistent with previous reports [13,22], which may be because the out-of-plane vibration mode of the topmost Te atoms is the most sensitive and may indicate the beginning of surface oxide formation.

3.2. The effect of SLO layer on the optical and electronic properties of WTe_2

The refractive index (n) and extinction coefficient (k) were fitted based on the Cauchy dispersion model for wavelengths above 1200 nm:

$$n(\lambda) = A + \frac{B}{\lambda^2} + \frac{C}{\lambda^4} \tag{4}$$

In this calculation, the following assumptions are made: WTe_2 naturally undergoes oxidation to form a composite of W-oxide and Te-oxide, which optically behaves as a dielectric material. As time progresses, the oxides accumulate in thickness, while the optical constants, derived from the Cauchy model, remain consistent. Once the optical constants for a particular thickness are ascertained, the corresponding thicknesses for other time measurements can be deduced. These measurements are carried out prior to the surface layer's oxidation, specifically when the oxide thickness is considered "0". To obtain smoother optical constants, we utilize the *Generalized Oscillator Model* within the ellipsometry software as a fitting function. The comprehensive results regarding the optical constants are presented in Fig. 1d, which provides a clear visualization of the relationship between the refractive index (n), extinction coefficient (k), and the wavelength. The absorption can be calculated with $\alpha = 4\pi k/\lambda$, the complex dielectric function (ε) can be obtained from $\varepsilon = 2n \cdot k$, as shown in Fig. 4.

To investigate the electronic properties of WTe_2 before and after oxidation, the KPFM mapping images of were measured comparatively, as shown in Fig. 5. WTe_2 was transferred on the top of electrodes with space of 5 μm. In panel (a), WTe_2 was exposure to the air, while in panel (b) WTe_2 was encapsulated by hBN film. The contact potential difference (CPD) between the sample and the KPFM tip is calculated using the following equation [35]:

$$CPD_{WTe2} = \frac{W_{Tip} - W_{WTe2}}{-e} \tag{5}$$

$$CPD_{SLO/WTe2} = \frac{W_{Tip} - W_{SLO/WTe2}}{-e} \tag{6}$$

where W_{tip}, W_{WTe2}, and $W_{SLO/WTe2}$ are the work function of the tip (Pt/Ir-coated Si), WTe_2, and SLO/WTe_2, respectively. The variation in CPD between WTe_2 and SLO/WTe_2 is given by

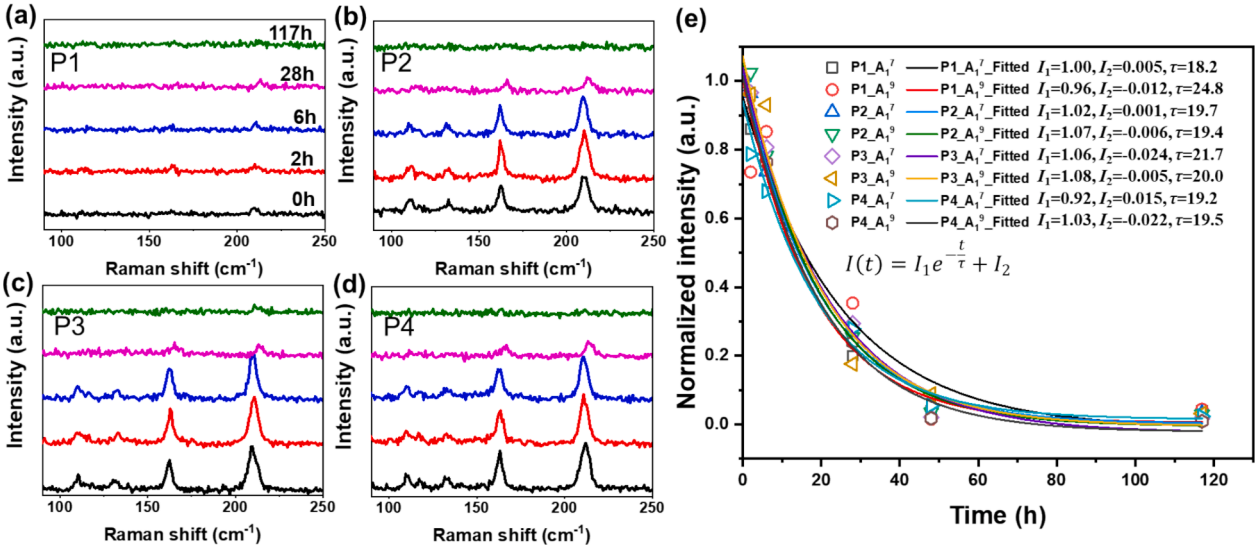

Fig. 3. (a-d) Evolution of Raman spectra of different thickness WTe_2 in ambient conditions. Measured Raman results of different thickness WTe_2 during degradation over 117 h. (e) Normalized intensities of peaks A_1^7 and A_1^9 vs time of different thickness WTe_2 during degradation over 117 h.

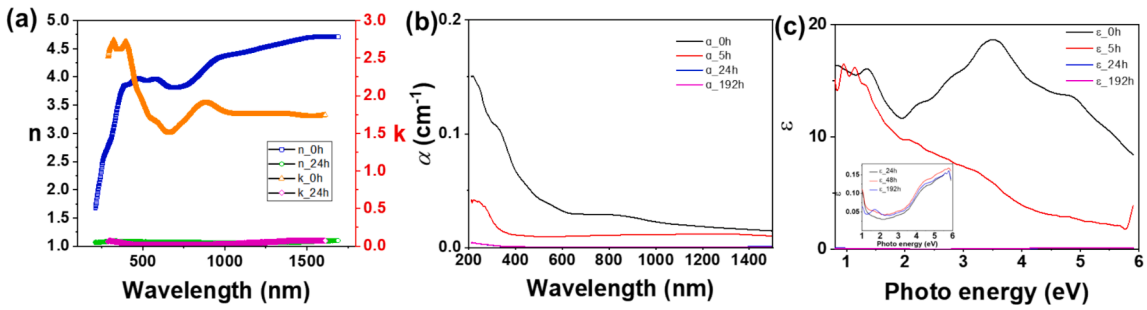

Fig. 4. (a) Optical constants for WTe_2 after exposure in the air for 24 h. The optical constants (n, k) for the WTe_2 were obtained by direct inversion of the ellipsometric values Ψ and Δ. (b) The adsorption coefficient (α) and (c) the imaginary part of the dielectric function (ε) of the WTe_2 after exposure in the air for 0, 5, 24, and 192 h.

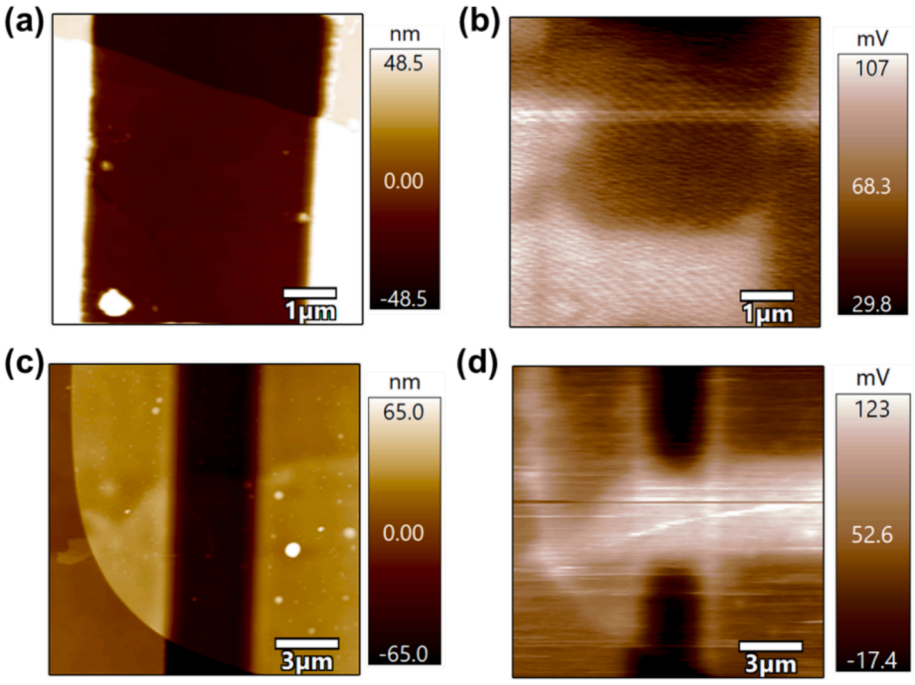

Fig. 5. Morphological images of (a) SLO/WTe_2 and (b) WTe_2 encapsulated by hBN film, and corresponding KPFM maps of (c) SLO/WTe_2 and (d) WTe_2.

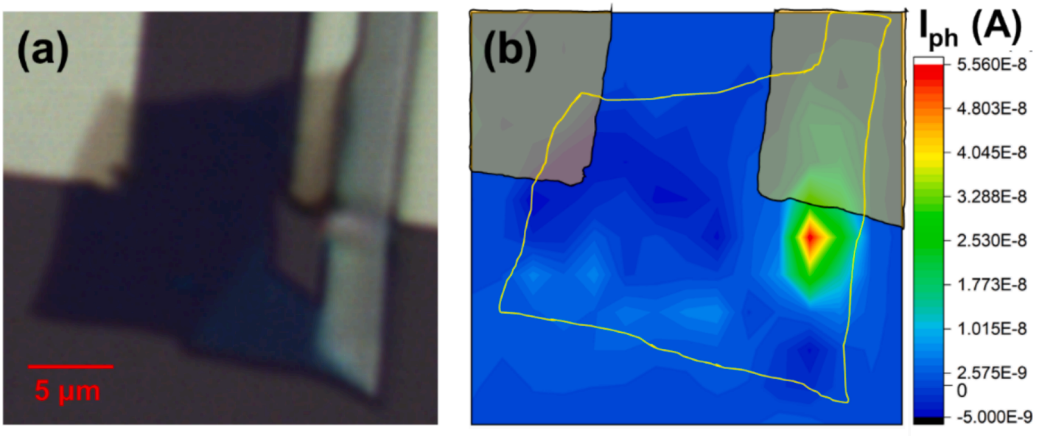

Fig. 6. a) Optical image of SLO/WTe_2 heterojunction device. b) Photocurrent mapping of SLO/WTe_2 heterojunction device under $V_{ds} = 0.1$ mV, and $P_{in} = 0.29$ mW, 532 nm laser. The excitation light was focused using a 100 × objective lens and the focused spot size was 3 μm. The yellow line indicates the area covered by the SLO/WTe_2.

$$\Delta CPD = CPD_{SLO/WTe2} - CPD_{WTe2} = \frac{W_{WTe2} - W_{SLO/WTe2}}{-e} = -144\ mV \quad (7)$$

From Fig. 5, it can be seen clearly observed that the surface potential of SLO/WTe_2 is ~144 mV smaller than that of WTe_2. Therefore, the Fermi level of SLO/WTe_2 is 144 meV higher than that of WTe_2. Oxidation alters the electronic structure and chemistry of the material's surface, thereby enhancing the electron binding. Moreover, the variation of the work function affects the energy band structure and electron transport properties of the SLO/WTe_2 heterojunction.

3.3. Photoresponse of SLO/WTe_2 heterojunction-based optoelectronic device

One few-layer WTe_2 was transferred onto Au electrodes and then naturally oxidized in the air, leading to the formation of the SLO/WTe_2 heterojunction device, as depicted in Fig. 6a. Photocurrent measurements were performed on the oxidized device by applying a bias voltage of 0.1 mV and utilizing a 532 nm laser with a power of 0.29 mW. Fig. 6b shows the corresponding photocurrent mapping image, revealing a peak photocurrent of 55.6 nA at the interface between the electrode and the SLO/WTe_2. This peak can be attributed to carrier accumulation due to the Schottky contact, a phenomenon well-documented in previous research on devices based on various 2D layered semimetals [8,23,24]. The regions exhibiting positive and negative photocurrents are broader compared to those in a standalone WTe_2 device. This broadening is due to the fact that, as indicated by AFM results in section 3.3, the work function of the SLO/WTe_2 heterojunction surpasses that of WTe_2. Consequently, the electron binding energy is stronger after oxidation, causing more photogenerated carriers to accumulate within the SLO layer, resulting in an expanded distribution of positive and negative photocurrents. It shows great potential for the applications of 2D WSMs materials in logical operations in ambient air.

3.4. Mechanism analysis of SLO/WTe_2 heterojunction-based device

According to the Raman test results, it is evident that the SLO layer, composed of $WTeO_x$ and TeO_2 [13,25], forms after 117 h. We investigate the band structure of pristine, partially oxidized, and fully oxidized WTe_2 monolayers. As shown in Fig. 7a-c, they are WTe_2, $WTeO_x$ and TeO_2, respectively. The energy band structure and the density of states (DOS), as illustrated in Fig. 7d and e, reveal that both WTe_2 and $WTeO_x$ exhibit semimetallic characteristics. Notably, the highest valence band of WTe_2 bends upwards while the lowest conduction band bends downwards forming an overlap of about 0.2 eV. This finding aligns with the observations made by Augustin *et al.* [26]. Upon full oxidation, TeO_2 forms, leading to a significant widening of the band gap.

Since the dielectric function and absorption coefficient play a crucial role in characterizing two-dimensional materials and their optical applications, we discussed the optical properties of WTe_2 monolayers, including pristine WTe_2, $WTeO_x$, and the fully oxidized product, TeO_2. The calculated imaginary part (ε_2) of the dielectric function and adsorption coefficient (α) of the WTe_2 monolayer is similar to the calculated result of Wei *et al.* [27], indicating the reasonableness of our calculations. As shown in Fig. 7, due to the forbidden transition between the valence band maximum (VBM) and the conduction band minimum (CBM), the two peaks of the ε_2 spectrum of the WTe_2 monolayer are located at 1.06 eV and 3.53 eV respectively, indicating that WTe_2 can achieve wide-spectrum light absorption from the ultraviolet to the infrared band. Upon partial oxidation, oxygen substitution shifts the ε towards the far infrared region, with peaks emerging at 0.99 eV and 3.47 eV. Following complete oxidation to form TeO_2, the change in crystal structure results in negligible infrared absorption and heightened ultraviolet light absorption. However, the ε_2 value after oxidation is lower than that of the monolayer WTe_2, indicating a weakened photon absorption capacity.

We compared the dielectric function and absorption coefficient of pristine WTe_2, $WTeO_x$, and TeO_2 with spectroscopic ellipsometry measurements conducted at 0 h, 5 h, 24 h, and 192 h. As illustrated in Fig. 8, the simulation and experimental results are in good agreement, indicating that after 24 h, the top layer transforms into TeO_2, exhibiting a preference for UV light absorption. This aligns with the ellipsometry test results. As the oxidation of WTe_2 progresses, the material's absorption coefficient decreases, and its absorption gradually narrows towards the UV band. This is attributed to TeO_2's bandgap of 3.6 eV, which enhances its responsiveness to UV light. Regarding the change in the dielectric function, the DFT calculation results at 0 h and the measured WTe_2 peaks both occur at 1 eV and 3.5 eV. Obviously, the intensity of the 3.5 eV peak diminishes significantly after 5 h, while the 1 eV peak rises, mirroring the $WTeO_x$ simulation results. This confirms that partial oxidation has indeed occurred at this stage. The 24 h and 192 h results are similar, indicating that oxidation reaches saturation after 24 h, and

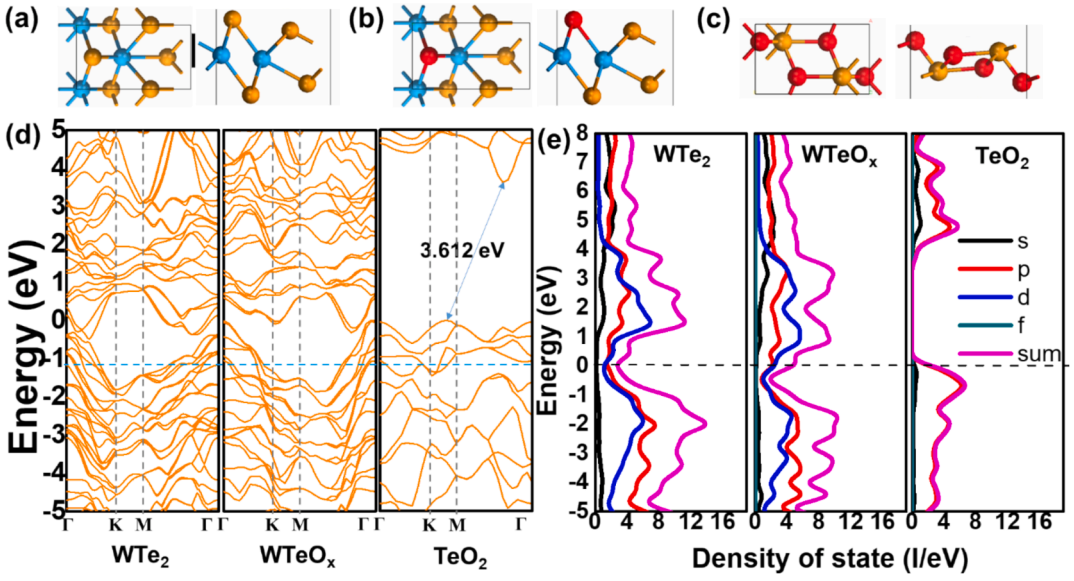

Fig. 7. Top and side views of the (a) pristine WTe_2, (b) partially oxidized WTe_2 ($WTeO_x$), and (c) fully oxidized WTe_2 (TeO_2). (d) Band structure and (e) density of state for WTe_2, $WTeO_x$, and TeO_2.

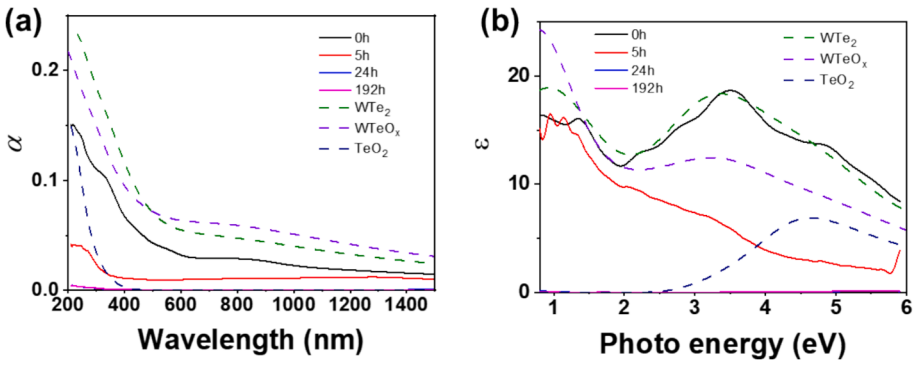

Fig. 8. (a) The adsorption coefficient (α) and (b) the imaginary part of the dielectric function (ε) of the pristine, partially oxidized, and fully oxidized WTe_2 monolayers. The solid lines represent the experimental results, and the dash line represent the DFT calculation results.

the dielectric function distribution shares characteristics with the $WTeO_x$ simulation results. Subsequently, the dielectric function distribution exhibits both WTe_2 and TeO_2 distributions, suggesting the formation of TeO_2 on the upper surface. It shows that the SLO layer has a significant effect on the optical and electronic properties, which is instructive for future wavelength-modulated device optoelectronic logic operations.

4. Conclusions

In this study, the effects of the self-limiting oxide (SLO) layer on the optical and electronic properties of WTe_2 and its implications for optoelectronic applications were investigated. Spectroscopic ellipsometry measurements showed that the oxide layer thickness on WTe_2 reaches saturation at around 10 nm after 45 h of atmospheric exposure, following a self-limiting oxidation process. Raman spectroscopy analysis of WTe_2 with different thicknesses before and after oxidation indicated the degradation behavior of the material, with decreasing peak intensities and red-shifted peak positions over time. The KPFM mapping images revealed that oxidation alters the electronic structure of WTe_2, increasing the Fermi level of SLO/WTe_2 compared to WTe_2. In the photocurrent tests of the SLO/WTe_2 heterojunction device, a wider distribution of positive and negative photocurrents was observed, suggesting potential applications in logical operations in ambient air. Density functional theory calculations further supported the understanding of the changes in the electronic and optical properties of WTe_2 due to oxidation. Overall, this research provides valuable insights into the role of the SLO layer on WTe_2 and offers guidance for the development of optoelectronic devices based on this material. Obviously, the SLO layer affects the optical and electronic properties significantly, which shows great potential in wavelength-modulated device optoelectronic logic operations. Future work could focus on optimizing the properties of the SLO/WTe_2 heterojunction to enhance device performance.

CRediT authorship contribution statement

Hongyu Tang: Writing – review & editing, Writing – original draft, Validation, Software, Methodology, Data curation, Conceptualization. **Weiqi Shi:** Software, Data curation. **Yifan Ding:** Validation, Data curation. **Jiao Qi:** Data curation, Software. **Shuai Wu:** Data curation, Methodology. **Weiming Liu:** Resources, Investigation. **Gaoyuan Wang:** Data curation. **Jiajie Fan:** Supervision. **Rongjun Zhang:** Supervision, Investigation. **Guoqi Zhang:** Supervision, Formal analysis.

Declaration of competing interest

The authors declare that they have no known competing financial interests or personal relationships that could have appeared to influence the work reported in this paper.

Acknowledgment

This study was supported by Shanghai Research Center for Silicon Carbide Power Devices Engineering &Technology Project [Grant No. 19DZ2253400].We thank Prof. Qingchun Zhang and Prof. Ruiqian Guo in Fudan University for their vigorous help of sample fabrications and measurements.

Data availability

Data will be made available on request.

References

[1] C. Tzschaschel, J.X. Qiu, X.J. Gao, H.C. Li, C.Y. Guo, H.Y. Yang, C.P. Zhang, Y. M. Xie, Y.F. Liu, A.Y. Gao, D. Berube, T. Dinh, S.C. Ho, Y.Q. Fang, F.Q. Huang, J. Nordlander, Q. Ma, F. Tafti, P.J.W. Moll, K.T. Law, S.Y. Xu, Nonlinear optical diode effect in a magnetic Weyl semimetal, Nat. Commun. 15 (2024).
[2] M.X. Cao, Z.H. Wang, L.W. Ma, L.W. Zhang, M. Wang, Y.S. Liu, J. He, X.L. Xi, Tungsten ditelluride: synthesis, structure, and magnetoresistance property, Adv. Electron. Mater. 7 (2021).
[3] Y. Okamura, S. Minami, Y. Kato, Y. Fujishiro, Y. Kaneko, J. Ikeda, J. Muramoto, R. Kaneko, K. Ueda, V. Kocsis, N. Kanazawa, Y. Taguchi, T. Koretsune, K. Fujiwara, A. Tsukazaki, R. Arita, Y. Tokura, Y. Takahashi, Giant magneto-optical responses in magnetic Weyl semimetal Co3Sn2S2, Nat. Commun. 11 (2020).
[4] J.E. Moore, Optical properties of Weyl semimetals, Natl. Sci. Rev. 6 (2019) 206–U243.
[5] A.N. Domozhirova, S. Naumov, A.A. Makhnev, E. Shreder, S.M. Podgornykh, E. B. Marchenkova, V.V. Chistyakov, J.C.A. Huang, V.V. Marchenkov, Galvanomagnetic and optical properties of type-II weyl semimetal candidate WTe2, IEEE T Magn. 58 (2022).
[6] Y. Pan, B. He, T. Helm, D. Chen, W. Schnelle, C. Felser, Ultrahigh transverse thermoelectric power factor in flexible Weyl semimetal WTe2, Nat. Commun. 13 (2022).
[7] B.R. Rano, I.M. Syed, S.H. Naqib, Elastic, electronic, bonding, and optical properties of WTe2 Weyl semimetal: a comparative investigation with MoTe2 from first principles, Results Phys. 19 (2020).
[8] Q.S. Wang, J.C. Zheng, Y. He, J. Cao, X. Liu, M.Y. Wang, J.C. Ma, J.W. Lai, H. Lu, S. Jia, D.Y. Yan, Y.G. Shi, J.X. Duan, J.F. Han, W.D. Xiao, J.H. Chen, K. Sun, Y. G. Yao, D. Sun, Robust edge photocurrent response on layered type II Weyl semimetal WTe2, Nat. Commun. 10 (2019).
[9] Y. Feng, Y. Zhang, Y. Zhang, X. Miao, Y. Lin, T. Min, Y. Pan, Self-powered broadband photodetectors based on large-scale continuous films of weyl semimetal WTe2, ACS Appl. Opt. Mater. 2 (2024) 333–340.
[10] Y.J. Liu, C. Liu, X.M. Wang, L. He, X.G. Wan, Y.B. Xu, Y. Shi, R. Zhang, F.Q. Wang, Photoresponsivity of an all-semimetal heterostructure based on graphene and WTe2, Sci Rep-Uk 8 (2018).
[11] J.N. Wang, H.Y. Wang, Q. Chen, L.G. Qi, Z.Q. Zheng, N.J. Huo, W. Gao, X.Z. Wang, J.B. Li, A Weyl semimetal WTe2/GaAs 2D/3D Schottky diode with high rectification ratio and unique photocurrent behavior, Appl. Phys. Lett. 121 (2022).
[12] C.H. Lee, E. Cruz-Silva, L. Calderin, M.A.T. Nguyen, M.J. Hollander, B. Bersch, T. E. Mallouk, J.A. Robinson, Tungsten ditelluride: a layered semimetal, Sci. Rep.-Uk 5 (2015).
[13] F. Hou, D.W. Zhang, P. Sharma, S. Singh, T. Wu, J. Seidel, Oxidation kinetics of WTe2 surfaces in different environments, Acs Appl. Electron. Ma. 2 (2020) 2196–2202.

[14] S.J. Clark, M.D. Segall, C.J. Pickard, P.J. Hasnip, M.J. Probert, K. Refson, M. C. Payne, First principles methods using CASTEP, Z. Kristallogr. 220 (2005) 567–570.
[15] H.J. Monkhorst, J.D. Pack, Special points for brillouin-zone integrations, Phys. Rev. B 13 (1976) 5188–5192.
[16] J.P. Perdew, K. Burke, M. Ernzerhof, Generalized gradient approximation made simple, Phys. Rev. Lett. 77 (1996) 3865–3868.
[17] F. Ye, J.S. Lee, J. Hu, Z.Q. Mao, J. Wei, P.X.L. Feng, Environmental instability and degradation of single- and few-layer WTe2 nanosheets in ambient conditions, Small 12 (2016) 5802–5808.
[18] M.K. Jana, A. Singh, D.J. Late, C.R. Rajamathi, K. Biswas, C. Felser, U. V. Waghmare, C.N.R. Rao, A combined experimental and theoretical study of the structural, electronic and vibrational properties of bulk and few-layer Td-WTe2, J Phys. Condens. Mat. 27 (2015).
[19] Y. Ding, W. Zheng, Y.M. Zhu, M.G. Jin, Z.G. Lin, R.N. Zhu, F. Huang, Raman tensor of layered Td-WTe2, J. Phys. Chem. C 124 (2020) 16596–16603.
[20] Y.C. Jiang, J. Gao, L. Wang, Raman fingerprint for semi-metal WTe2 evolving from bulk to monolayer, Sci. Rep.-Uk 6 (2016).
[21] Q.J. Song, X.C. Pan, H.F. Wang, K. Zhang, Q.H. Tan, P. Li, Y. Wan, Y.L. Wang, X. L. Xu, M.L. Lin, X.G. Wan, F.Q. Song, L. Dai, The in-plane anisotropy of WTe2 investigated by angle-dependent and polarized raman spectroscopy, Sci Rep-Uk 6 (2016).
[22] E.Z. Zhang, R. Chen, C. Huang, J.H. Yu, K.T. Zhang, W.Y. Wang, S.S. Liu, J.W. Ling, X.G. Wan, H.Z. Lu, F.X. Xiu, Tunable positive to negative magnetoresistance in atomically thin WTe2, Nano Lett. 17 (2017) 878–885.
[23] J.C. Ma, Q.Q. Gu, Y.N. Liu, J.W. Lai, P. Yu, X. Zhuo, Z. Liu, J.H. Chen, J. Feng, D. Sun, Nonlinear photoresponse of type-II Weyl semimetals, Nat. Mater. 18 (2019) 476-+.
[24] J.W. Lai, X. Liu, J.C. Ma, Q.S. Wang, K.A. Zhang, X. Ren, Y.A. Liu, Q.Q. Gu, X. Zhuo, W. Lu, Y. Wu, Y. Li, J. Feng, S.Y. Zhou, J.H. Chen, D. Sun, Anisotropic broadband photoresponse of layered type-II Weyl semimetal MoTe2, Adv. Mater. 30 (2018).
[25] J.L. Yang, Y.J. Jin, W.P. Xu, B.B. Zheng, R. Wang, H. Xu, Oxidation-Induced Topological Phase Transition in Monolayer 1T′-WTe2, J Phys Chem Lett, 9 (2018) 4783-+.
[26] J. Augustin, V. Eyert, T. Böker, W. Frentrup, H. Dwelk, C. Janowitz, R. Manzke, Electronic band structure of the layered compound Td-WTe2, Phys. Rev. B 62 (2000) 10812–10823.
[27] J.-W. Wei, Z.-W. Ma, H. Zeng, Z.-Y. Wang, Q. Wei, P. Peng, Electronic and optical properties of vacancy-doped WS2 monolayers, AIP Adv. 2 (2012) 042141.